









High saturation photocurrent THz waveguide-type MUTC-photodiodes reaching mW output power within the WR3.4 band

MARCEL GRZESLO,^{1,*}  SEBASTIAN DÜLME,^{1,2} 
SIMONE CLOCHIATTI,³ TOM NEERFELD,¹ THOMAS HADDAD,¹ 
PENG LU,¹  JONAS TEBART,¹ SUMER MAKHLOUF,¹ 
CARLOS BIURRUN-QUEL,⁴  JOSÉ LUIS FERNÁNDEZ ESTÉVEZ,¹
JÖRG LACKMANN,¹ NILS WEIMANN,³ AND ANDREAS STÖHR^{1,5}

¹University of Duisburg-Essen, Optoelectronics, Lotharstr. 55, 47057 Duisburg, Germany

²now with RPG Radiometer physics GmbH, Werner-von-Siemens-Str. 4, 53340 Meckenheim, Germany

³University of Duisburg-Essen, Components for High Frequency Electronics, Lotharstr. 55, 47057 Duisburg, Germany

⁴Universidad Pública de Navarra, Campus de Arrosadía, 31006, Pamplona, Navarra, Spain

⁵Microwave Photonics GmbH, Essener Str. 5, 46047 Oberhausen, Germany

*marcel.grzeslo@uni-due.de

Abstract: In this paper, we report on waveguide-type modified uni-traveling-carrier photodiodes (MUTC-PDs) providing a record high output power level for non-resonant photodiodes in the WR3.4 band. Indium phosphide (InP) based waveguide-type 1.55 μm MUTC-PDs have been fabricated and characterized thoroughly. Maximum output powers of -0.6 dBm and -2.7 dBm were achieved at 240 GHz and 280 GHz, respectively. This has been accomplished by an optimized layer structure and doping profile design that takes transient carrier dynamics into account. An energy-balance model has been developed to study and optimize carrier transport at high optical input intensities. The advantageous THz capabilities of the optimized MUTC layer structure are confirmed by experiments revealing a transit time limited cutoff frequency of 249 GHz and a saturation photocurrent beyond 20 mA in the WR3.4 band. The responsivity for a 16 μm long waveguide-type THz MUTC-PD is found to be 0.25 A/W. In addition, bow-tie antenna integrated waveguide-type MUTC-PDs are fabricated and reported to operate up to 0.7 THz above a received power of -40 dBm.

© 2023 Optica Publishing Group under the terms of the [Optica Open Access Publishing Agreement](#)

1. Introduction

Nowadays, high-speed photodiodes (PDs) have become a key component for several photonic millimeter-wave and terahertz applications [1]. Due to their high output power and wideband capabilities up to the THz-region, they are used as transmitters for communication, spectroscopy, imaging, or sensing applications [2–5]. For free-space applications, high-speed single PDs or arrays of PDs are integrated with resonant or wideband planar antennas for various systems like THz imaging or beam steering [6–10]. As an alternative to free-space antennas, coplanar waveguides (CPWs) are used, e.g. for integrating PDs with additional active or passive devices like amplifiers, mixers, capacitors, or filters. Also, CPW based antenna transitions offer an integration of PDs with standard rectangular waveguides (WR) interfaces, which are often used in radar and communication applications [10].

Introduced in 1997 from Ishibashi et al., uni-traveling carrier photodiodes (UTC-PDs) have shown a breakthrough in terms of high-speed and high output power [11]. These devices were based on a combination of pin-PDs and hetero junction bipolar transistors. The main invention was to bring in a highly doped p-absorber, to suppress the transport of holes that exhibit a

higher effective mass than electrons. Therefore, predominantly high mobility electrons are drifting, reducing the junction transit time and thus improving the photodiodes' high-frequency performance. To further reduce transit time limitations in UTC-PDs, velocity overshoot in conjunction with precise E-field management in the various layers of the photodiode's structure have been exploited [12]. For a systematic optimization of overshoot effects and the photodiode's bandwidth, advanced simulation tools like the energy-balance (EB) model, which takes non-equilibrium transport dynamics of electrons into account were introduced [13,14].

In the last twenty years, many variants of the original UTC-PDs have been presented. By adding non-intentionally doped additional absorber layers, modified UTC-PDs (MUTC-PDs) or triple transit region PDs (TTR-PDs) were reported [15–20]. These modified structures show beneficial properties especially in terms of carrier transitions time and power saturation [15]. Key aspects of the various variants include additional cliff-layers, graded doping composition, or non-uniform doping profiles for optimizing the E-field distribution in the different layers of the photodiode epitaxial structure [16]. In addition to the junction layout, the type of optical coupling greatly impacts the PD performance. For increasing the RC-cutoff frequency, the active area of the photodiodes needs to be reduced. For vertically illuminated PDs, this is only limited by the spot-size of the incident light beam. Nevertheless, vertical transmission provides rather low responsivities due to the thin absorption layers used in most UTC-PD designs. A sophisticated approach to overcome this limitation uses a refractive facet, which leads to a quasi-vertical coupling with a slightly increased absorbing length [21]. Other possibilities include the use of optical resonant metal contacts, which confine the optical wave in proximity to the active region [22]. Yet another concept describes so-called traveling-wave (TW) UTC-PDs, which aim to match the group velocity of the optical wave to the phase velocity of the generated RF-signal [23,24].

In contrast to these vertical approaches, waveguide PDs (WG-PDs) typically show higher responsivities. This is mainly because the size and thickness of the absorbing layer of the PD can be reduced independent of the optical waveguide coupling. This is achieved by adding a passive optical waveguide (POW) and utilizing evanescent optical coupling from the POW into the active region of the PD [25]. This facilitates an efficient generation of photocurrents while maintaining a rather uniform current density. However, there is a trade-off between saturation output power and RC-limited 3 dB bandwidth. For reasonable optical coupling efficiencies, comparably long PDs are required, which in turn leads to a higher junction capacitance preventing the fabrication of PDs with a 3 dB cutoff frequency in the THz range.

In this paper, we report waveguide-type MUTCs in contrast to most reported THz-PDs, which aimed at reducing the size of the PDs. Despite the lower 3 dB cutoff frequencies for longer WG-PDs, higher THz output power levels are achieved by increasing the saturation photocurrent of the photodiodes. By modifying the doping profile of the MUTC-PD layer structure and introducing specific cliff layers, precise E-field management across the layer structure is achieved. This supports fast carrier transport and compensates charge carrier screening effects at very high optical input powers. Adapted from the optimized InP-based layer structure, broadband 1.55 μm waveguide MUTC-PDs featuring a planar integrated 50 Ω CPW output were fabricated exhibiting a high saturation photocurrent level. At 240 GHz, the saturation photocurrent and maximum output power for a 17 μm long waveguide MUTC-PD is 21 mA and -0.6 dBm. To our knowledge, a similar high output power has only been achieved using a temperature controlled TW-UTC-PD reaching -0.7 dBm at 220 GHz [26]. Furthermore, to experimentally confirm the numerically determined transit time limitations, bowtie (BT) antenna integrated waveguide MUTC-PDs were fabricated and tested for frequencies up to 0.7 THz.

2. Photodiode junction design

The layout of the photodiode's junction layers consists of a hybrid InGaAs absorber with a depleted and undepleted section, which is placed as a sandwich between two regions of InP. In Table 1, the epitaxial layout of the WG-PDs is summarized. The highly doped p-type InP layers on top are used as diffusion blocker, while the lower undoped InP layer functions as the depleted collector and cladding for the waveguide. Energy band discontinuities are smoothed by InGaAsP spacer layers at both hetero junctions. To further support the transition of electrons into the collector, an inhomogeneous doping profile is implemented by inserting several cliff layers in the absorber as well as in the collector region. For the p- and n-contact layers, p⁺-InGaAs and n⁺-InP are used, respectively.

Table 1. Epitaxial layers of waveguide MUTC-PD

Material	THICKNESS (NM)	DOPING (CM ⁻³)	Function
InGaAs	50	Zn: 2·10 ¹⁹	p-contact layer
InP	500	Zn: 1.5·10 ¹⁸	Diffusion block
InGaAsP Q1.10	10	Zn: 2·10 ¹⁸	Spacer
InGaAsP Q1.40	10	Zn: 2·10 ¹⁸	Spacer
InGaAs	50	Zn: 2·10 ¹⁸ - 2·10 ¹⁷	Undepleted absorber
InGaAs	40	Zn: 1·10 ¹⁷	Depleted absorber
InGaAs	10	Zn: 4·10 ¹⁷	p-cliff
InGaAs	10	n.i.d.	Spacer
InGaAsP Q1.50	10	n.i.d.	Spacer
InGaAsP Q1.15	10	n.i.d.	Spacer
InP	10	Si: 5·10 ¹⁷	n-cliff
InP	40	Si: 5·10 ¹⁶	Compensated collector 1
InP	100	Si: 1·10 ¹⁶	Compensated collector 2
InGaAsP Q1.25	350	Si: 1.5·10 ¹⁸	Waveguide core
InP	1.000	Si: > 1·10 ¹⁹	n-contact layer
InP	100.000	Fe-compensated	Substrate

Resulting from EB-simulations, Fig. 1 illustrates the E-field distribution in Fig. 1(a) and average electron velocity (Fig. 1(b)) across the layer structure. In this simulation, the PD was set to 1.2 V reverse with a constant optical intensity of 0.6 MW/cm² resulting in a current density of 55 kA/cm². These simulations were carried out using a technology computer-aided design (TCAD) software from Silvaco ATLAS. For determining the carrier dynamics, both low field and high field mobility models were applied, latter considering the redistribution of heated carriers into nearby valleys, which reduces the overall mobility. This process takes place within the energy relaxation time, leading to a reduced average velocity of electrons during this transition, referred to as an “overshoot” [13].

Due to the precise E-field across the absorber, a pronounced overshoot is achieved, leading to an improved overall transit time limited 3 dB frequency of about 254 GHz. Besides improving the transit time 3 dB frequency, the increased average velocity suppresses carrier screening effects in the interface region between the InGaAs absorber and the InP collector. As can be seen from Fig. 1(a), the overall electric field decreases at high optical intensities. However, due to the charge compensating layers within the collector even for 0.6 MW/cm² the field does not fall below the critical value of 11 kV/cm in InP regarding the negative differential mobility [27]. This leads to higher saturation photocurrents and therefore to a higher possible RF-output power level.

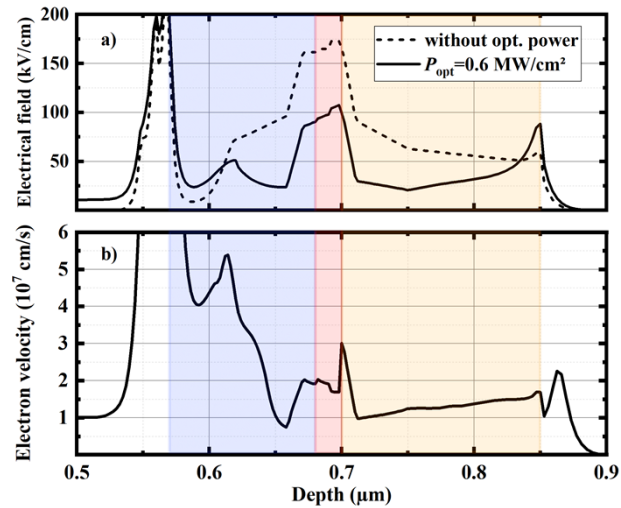


Fig. 1. Simulated electric field distribution in a) and the corresponding average electron velocity profile in b) at 1.2 V reverse bias and an optical intensity of 0.6 WM/cm². The dashed line shows the initial electrical field distribution when no illumination is present.

3. Fabrication

The layer structure of the MUTC-PD was grown by metal organic chemical vapor deposition (MOCVD) on a two inch iron compensated indium phosphide wafer. The photodiodes were fabricated via a standard photolithography process and wet chemical mesa etching. The schematic process flow in Fig. 2 illustrates the fabrication steps. The production of the PDs begins with the metallization of the p-contacts (step I), composed of Ti/Pt/Au layers (30 nm/70 nm/400 nm). Afterwards, the p- and n-mesas were formed by wet chemical etching. Selective etching of InP and InGaAs/InGaAsP was achieved using a 37% hydrochloric acid (HCl/H₂O) and a phosphoric acid - hydrogen peroxide - water mixture (1:1:5; H₃PO₄/H₂O₂/H₂O), respectively (step II). The passive optical waveguide was created by a tailored under-etching process. Using a structured photoresist with 13 μm width, roughly 2.5 μm wide POWs were fabricated. In a second metallization process, Ni/Ge/Au (10 nm/10 nm/400 nm) contacts were deposited on top of the n-mesa (step III).

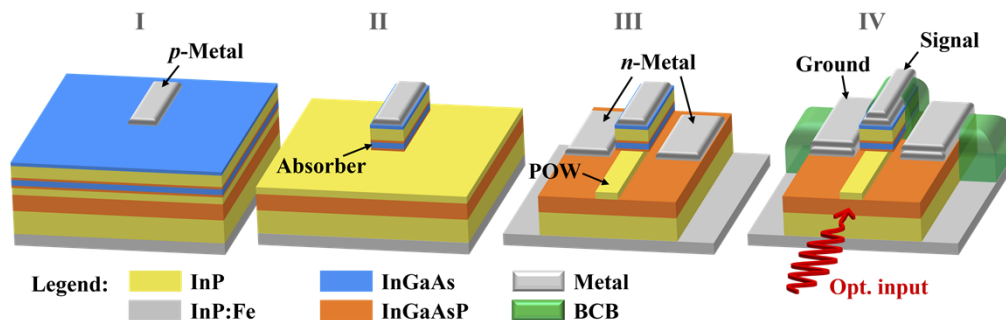


Fig. 2. Schematic process flow illustrating the fabrication of the waveguide photodiode.

To achieve low contact resistances, both metals were annealed at 360° C for two minutes. Specific contact resistances have been determined by TLM-measurements and were found to be as low as $2 \cdot 10^{-6} \Omega/\text{cm}^2$ and $6 \cdot 10^{-7} \Omega/\text{cm}^2$ for p- and n-contacts, respectively. Diluted

benzocyclobutene (BCB) was used for isolation and passivation of the mesas. A following baking-step at 300 °C for 2 h has decreased the water content of the BCB and smoothed the edges. Ground-signal-ground (GSG) CPW with 35 μm signal and 25 μm gap width were fabricated by another Ti/Au deposition (step IV). Beside the CPW-structures, antenna apertures for antenna-integrated PDs were also deposited in this process step. To reduce RF-losses due to substrate modes, the iron-compensated InP substrate was thinned down to 100 μm via lapping. An optical microscope picture of a fabricated 17 μm long CPW-integrated PD is depicted in Fig. 3(a). A scanning electron microscope (SEM) picture of a shorter PD in Fig. 3(b) reveals a closer view of the coupling region and the characteristically under-etched InP diffusion-block layer. The possibility to reduce the junction area while maintaining a rather large p-contact provides a low capacitance and a low series resistance, both minimizing the RC-limitation.

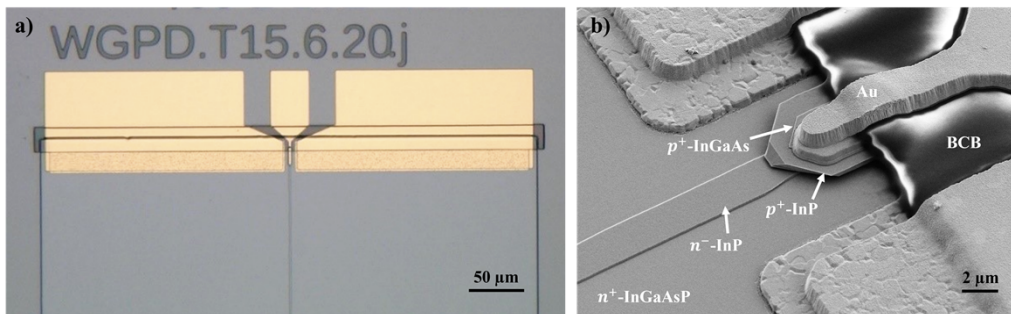


Fig. 3. Optical microscope picture a) and SEM-picture b) of fabricated CPW-integrated waveguide-type UTC-Photodiodes with length of 17 μm and 7 μm respectively.

4. Experimental characterization

4.1. DC and CV characteristics

The following measurements reveal some general diode properties like the dark current or the capacitance. Current-voltage (IV) curves of the fabricated MUTC-PD are depicted in Fig. 4 for different device dimensions. Under normal light conditions in the laboratory, dark currents of about 10 nA are measured at -4 V, which represent quite low leakage currents.

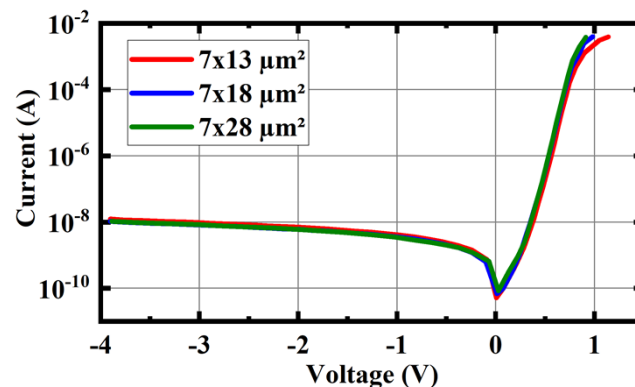


Fig. 4. DC-measurements of the diode characteristics for several photodiode areas.

For further investigations, CV-characteristics at 1 MHz were measured by an LCR meter. The extracted capacitances are shown in Fig. 5 as a linear trend with an offset indicating the parasitic capacitance. Subtracting the contribution of the parasitic capacitances reveals a very good agreement with theoretical calculations of the junction capacitances. The offset of the linear trend reveals the rather high parasitic capacitance of about 12 fF, which is mostly caused by the stray fields of the CPW-transition. This contribution reduces the performance of the frequency response dramatically and basically halves the bandwidth of a PD with an area of about $30 \mu\text{m}^2$. This statement is further consolidated by vector network analysis of the fabricated MUTC-PDs summarized in the following section.

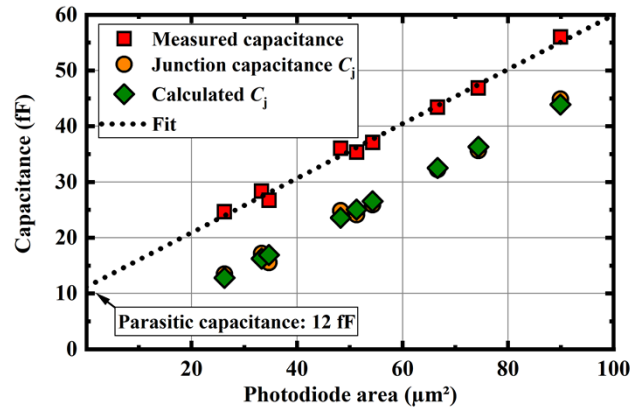


Fig. 5. Measured junction capacitances revealing the parasitic capacitance contributed by the tapered CPW-transition.

4.2. Network analysis and circuit fitting

The output power of the MUTC-PD experiences additional losses contributed by the complex impedance of the device. By defining suitable equivalent circuits it's possible to approximate the frequency-dependent behavior of the PD's junction regions, the series resistance and capacitances or inductances of the transmission line. By analyzing the contribution of each component, it is possible to deembed the loss characteristic of the external circuit and reveal the performance of the PD itself.

In this work, the active region of the PD has been partitioned into three RC segments like approaches used in prior publications, which established an accurate analytical description of the frequency dependent impedance [28,29]. Besides describing the RC-characteristic of the PD, the approach is also useful to approximate the transit time related time delay as a separate parallel equivalent circuit consisting of a capacitance C_t and a series resistance R_t [30]. Since the transit time limited 3 dB frequency of the PDs shown in this work exceeds the RC-limitation and the bandwidth of the employed network analyzer by far, its contribution will not be included in the fitting process of the equivalent circuit. However, the effect of the transit time limitation can be extracted from ultra-broadband frequency response measurements, as will be shown in chapter 4.5. The applied equivalent circuit is illustrated in Fig. 6(a). It includes the transit time delay at port 1 (left blue frame), the intrinsic RC characteristic of the MUTC-PD (right blue frame), the contribution of the contact resistance and stray fields (red frame) and as well as the contribution of the CPW transition at port 2 (green frame).

The equivalent circuit of the internal MUTC-PD can be further subdivided into the active junction region, which corresponds to the complex impedance obtained from TCAD. Here the junction resistances $R_{j,i}$ and capacitances $C_{j,i}$ correspond to the individual absorber, spacer, and

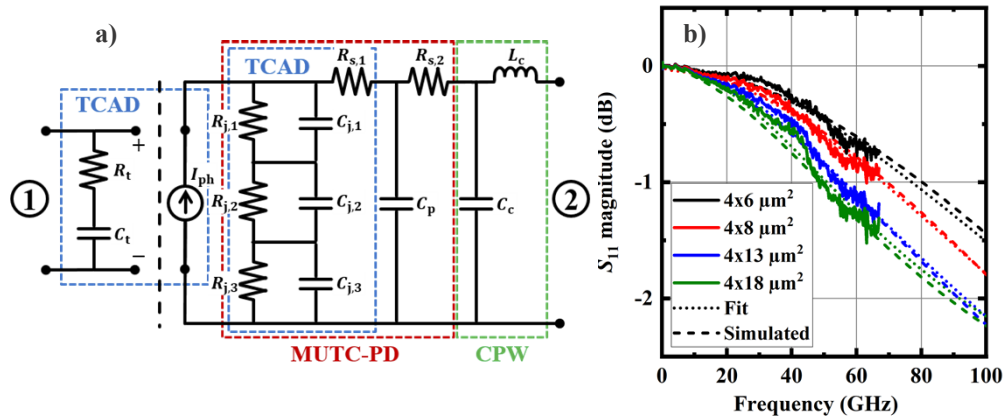


Fig. 6. Equivalent circuit including transit time and RC characteristic at port 1 and port 2 respectively in a) and S-parameter characterization of several photodiode geometries in b) showing the corresponding fitting curves of port 2.

collector layers. The series resistance was separated in bulk resistance $R_{s,1}$ and contact resistance $R_{s,2}$, which are mostly contributed by the p-contact region of the PD. The scattering parameters were measured up to 67 GHz using a network analyzer (Rohde & Schwarz ZVA67). Standard open/short/load (OSL) calibration has been carried out in advance using an on-wafer calibration kit to ensure reproducible results.

A comparison between the measured magnitude scattering-parameters, the fitted equivalent circuit, and simulations for several PD geometries with a reverse bias of 1 V are shown in Fig. 6(b). As can be seen, there is a good agreement between the fitted curves (dotted line) and simulated S_{11} magnitude (dashed lines). The magnitude, phase as well as real and imaginary part of the PD's impedance are shown in Fig. 7. for a PD area of $4 \times 18 \mu\text{m}^2$. Also, simulation results obtained from TCAD are included in Figs. 7 to allow for comparison. As can be seen, there is a reasonably good agreement between the measurements and the simulations.

The junction resistance and capacitance determined from the measurements in Figs. 6 are summarized in Table 2 for various PDs with different geometries. These fitted junction capacitances C_j , which were calculated from the individual junction capacitances $C_{j,1}$, $C_{j,2}$ and $C_{j,3}$ in series, are in very good agreement with the measured values shown above in Fig. 5.

Table 2. Exemplary results from the fitted equivalent circuit

PD geometry (μm^2)	R_j (k Ω)	C_j (fF)	$C_{j,1}$ (fF)	$C_{j,2}$ (fF)	$C_{j,3}$ (fF)	$R_{s,1}$ (Ω)	$R_{s,2}$ (Ω)	C_p (fF)	f_{RC} (GHz)	$f_{RC,eq}$ (GHz)	ρ_c (Ωcm^2)
4×6	10.0	14.7	33.6	112	34.1	5.0	22.6	1.5	76.7	139.0	$4.07 \cdot 10^{-6}$
4×8	4.3	16.5	64.1	49	40.5	5.3	19.8	0.9	74.3	128.2	$4.75 \cdot 10^{-6}$
4×13	3.2	27.6	77.9	372	48.3	3.6	11.5	1.3	61.7	88.5	$4.49 \cdot 10^{-6}$
4×18	2.7	38.3	102.3	367	73.5	2.6	8.1	1.5	52.2	68.5	$4.37 \cdot 10^{-6}$

Using the extracted contact resistances and the given contact geometries it is also possible to estimate the specific contact resistivities, which are in a range between $4 \cdot 10^{-6} - 5 \cdot 10^{-6} \Omega\text{cm}^2$. Due to the rather large area of the n-contact, the contact resistivity is attributed to the p-contact.

In the following, the fitted values are embedded into TCAD simulations in order to study the transient carrier dynamics regardless of the lateral PD topology. This allows analyzing the RC-frequency limitation of the active PD section (red frame in Fig. 6(a) independent of the impact of the CPW-transmission line, which itself exhibits a parasitic capacitance of 12 fF as

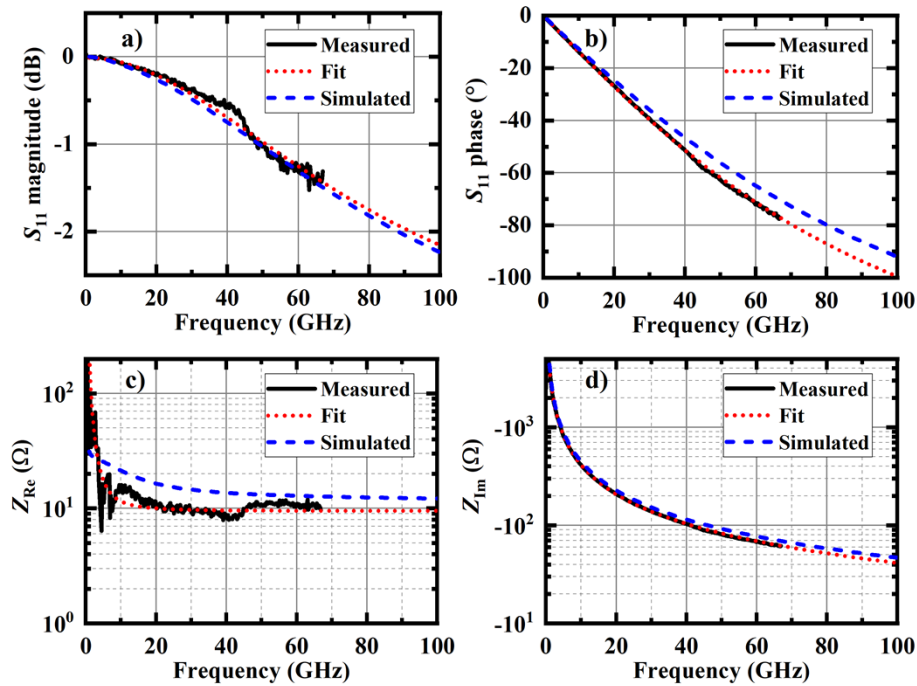


Fig. 7. Obtained scattering parameters of the photodiode with a geometry of $4 \times 18 \mu\text{m}^2$ in comparison with the fitted equivalent circuit and simulation in a) and b). The corresponding impedance values are shown in c) and d).

mentioned in Section 4.1. As an example, for a PD with an area of $4 \times 6 \mu\text{m}^2$, the cutoff frequency of the internal MUTC-PD was determined to be 139 GHz while the measured cutoff frequency is only 76.7 GHz due to the impact of the CPW.

4.3. Optical characteristics

The measured responsivities of fabricated MUTC-PDs are shown in Fig. 8 versus the diodes' lengths. A maximum responsivity of ~ 0.28 A/W was obtained for devices with lengths greater than $16 \mu\text{m}$. This includes average optical coupling losses into the photodiodes with no anti-reflection coating and propagation losses in the POW of about 4.8 dB in total. The maximum responsivity of the fabricated photodiodes depends on the periodic behavior of the optical evanescent coupling and optical losses in the POW and thus does not substantially increase even for longer diodes.

This phenomenon is in excellent agreement with optical FDTD simulations using Ansys Lumerical from which the effective coupling length is determined to be about $9 \mu\text{m}$, which leads to an absorption efficiency of about 63% for a $16 \mu\text{m}$ long photodiode. Due to the evanescent optical coupling and absorption, the optical intensity along the waveguide length is inhomogeneous. This leads to the effect that although shorter photodiodes provide a better RC-time constant than longer ones, saturation occurs at a significantly smaller photocurrent level. This will be explained in more detail in the following section. To achieve a high optical coupling efficiency, the width of the optical waveguide was kept wider than $2 \mu\text{m}$ as optical propagation loss increases at lower widths. Furthermore, the waveguide core height was adjusted to achieve phase matching between the modes in the waveguide and absorber region. The InP collector thickness was fixed at 150 nm, representing a trade-off between a short coupling length and RC limitation.

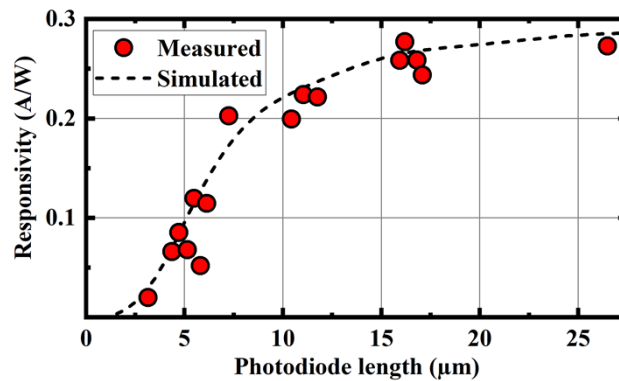


Fig. 8. Experimentally extracted responsivities (circles) and the theoretical responsivity (dashed line) in dependency of the photodiode length obtained by optical FDTD simulations.

4.4. RF-characteristics of CPW-PDs

The RF-capabilities of the PDs were characterized using an optical heterodyne setup. By combining the output power of two commercial C-band tunable external cavity laser diodes, the required optical beat signals were generated. With a lensed optical fiber, the optical signal was coupled into the facet of the optical waveguide. For on-chip probing from DC to 320 GHz, different GSG RF-probes were used. For DC to 110 GHz, a RF-probe with 1 mm-connector output was used and connected to an RF-power meter (Rohde & Schwarz NRP-Z58). For higher frequencies, WR5 (140-220 GHz) and WR3.4 (220-330 GHz) band RF-probes and Virginia Diodes (VDI) Schottky barrier diodes (SBD) were used. The calibration of the SBDs were provided by the manufacturer. The RF-power generated by the photodiodes were determined from the measured values after deembedding the RF-losses of the probes and RF-cables for the DC to 110 GHz measurements.

Figure 9(a) shows the normalized frequency response of up to 320 GHz for three PDs with different geometries. All PDs were reverse biased at -1.2 V. To allow for comparison, all measurements were carried out at small photocurrent levels well below saturation. From Fig. 9(a), the RC penalty for larger PDs compared to the smaller ones can be clearly observed at higher frequencies. The theoretically determined curves that are also included in Fig. 9(a) were simulated using the EB model described in Section 2. Here, the impedance of the diodes and the impact of the CPW are also considered. As can be seen, there is a good agreement between the measured and simulated frequency responses. As expected, the RC limitation scales with the junction area. However, it should be mentioned here that also the specific contact resistivity has a strong impact on the frequency response, as will be explained in detail further below. Absolute output power measurements across the WR3.4 band are shown in Fig. 9(b) for a PD with a geometry of $2 \times 9 \mu\text{m}^2$ at 5 mA photocurrent. For comparison, a WR3.4-SBD detector and a calorimeter (PM5B from VDI), both calibrated by the manufacturers, were used. Power measurements carried out with the SBD show strong power fluctuations of ± 3 dB over frequency which are most likely caused by standing waves. The saturation output power level shown below in Fig. 9(b) were measured using the PM5B.

At this point it should be noted that transit time limitations cannot be easily identified from Fig. 9(a) or (b). Despite transit time limitations of around 250 GHz determined from simulations, additional effects such as penalties due to substrate modes are also present. For experimentally determining the transit time, the frequency response of a bow-tie antenna integrated PD was characterized up to 1.2 THz. These results will be presented in Section 4.5.

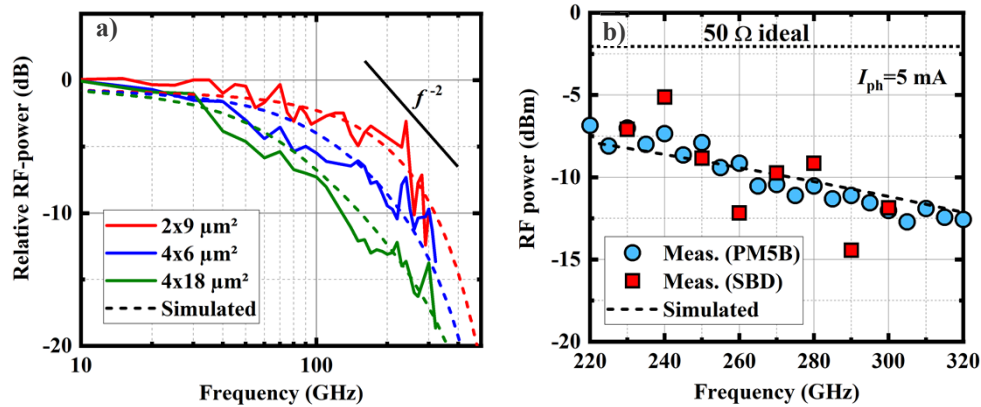


Fig. 9. Measured and simulated relative RF-response until 320 GHz for several photodiode geometries in a). The absolute RF-response of the photodiode with $2 \times 9 \mu\text{m}^2$ is shown in b). Here both a WR3.4-SBD (red squares) and a calorimeter (PM5B) (blue circles) from VDI were used to validate the accuracy of the absolute PD power within the WR3.4 band. The RC-limitation in the simulations (dashed lines) has been adjusted for the measured junction capacitances and series resistances obtained by fitting the equivalent circuit.

In Fig. 10, the simulated frequency responses are shown as a function of the PD length for a $4 \mu\text{m}$ wide (blue lines) and a $2 \mu\text{m}$ wide (red lines) junction. Furthermore, the fitted 3 dB cut-off frequencies for the measured PDs from Fig. 9(a) are also shown in Fig. 10 as circles. The analytic RC-model includes RC- as well as transit time limitations. The model also considers the influence of the contact resistivity ρ_c . According to TLM and S-parameter measurements, the contact resistivity of the fabricated MUTC-PDs varies, which is traced back to an inhomogeneous thickness of the p-InGaAs contact layer across the wafer and p-contact misalignments. As can be seen from Fig. 10, the fitted 3 dB cut-off frequency of the measured $2 \mu\text{m}$ and $4 \mu\text{m}$ wide PDs are in good agreement to the simulated curves for $2 \cdot 10^{-6} \Omega\text{cm}^2$ and $5 \cdot 10^{-6} \Omega\text{cm}^2$, respectively.

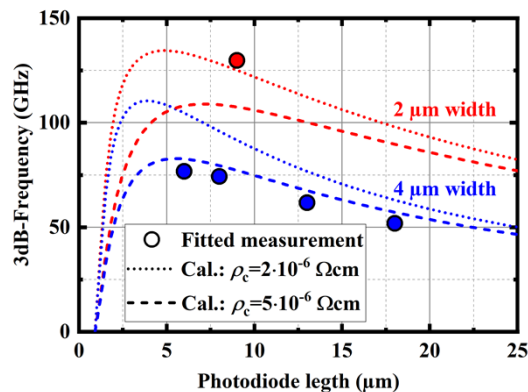


Fig. 10. Measured cutoff frequencies obtained from response fitting in comparison with analytical calculations in dependency of the photodiodes' length and widths for $4 \mu\text{m}$ (blue circles) and $2 \mu\text{m}$ (red circle). Additionally, the influence of a varying contact resistivity ρ_c is shown in the calculation with $2 \cdot 10^{-6} \Omega\text{cm}^2$ (dotted curves) and $5 \cdot 10^{-6} \Omega\text{cm}^2$ (dashed curves).

As mentioned in Section 2, an improvement of the transit time limited frequency can be achieved by adjusting the electric field profile, which can be influenced by setting the reverse bias voltage. The ideal bias point was evaluated by sweeping the bias at different frequencies. As Fig. 11(a) shows, the optimum bias lies in the range between -0.8 V and -1.5 V for a PD with a geometry of $2 \times 9 \mu\text{m}^2$ for low photocurrents without saturation taking place.

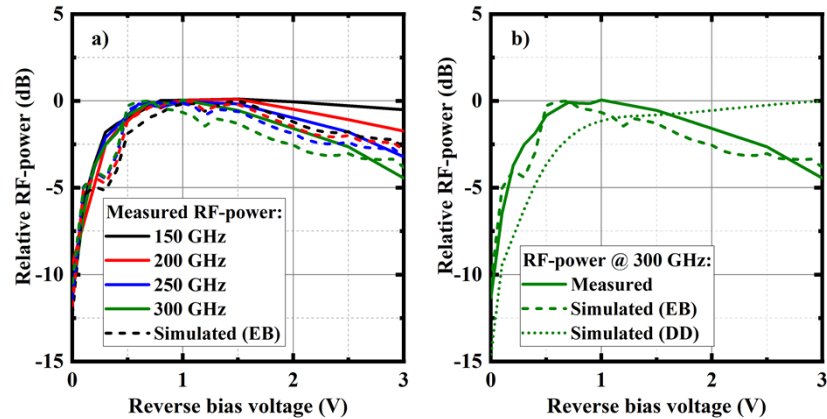


Fig. 11. Measured (continuous) and simulated (dashed lines) RF-power in dependency of bias for several frequencies in a) and at 300 GHz in b). The PD features an area of $2 \times 9 \mu\text{m}^2$ and was set to a photocurrent where no saturation was present. The EB-simulated voltage range for maximal output power matches well with the measurements using the while DD-simulations (dotted line) exhibit no optimal bias.

For frequencies above 150 GHz the output power or overall cutoff frequency decreases at higher negative voltages indicating a reduced average carrier velocity. An increase in average velocity around -1 V most likely results from an improved electric field distribution in which electrons maintain their non-equilibrium average velocity over a longer distance.

Both phenomena are in good agreement with our EB model simulations whereas the drift diffusion (DD) simulations in Fig. 11(b) just take the saturation velocity into account, which charge carriers acquire when reaching equilibrium. This reveals a much less distinct improvement in average velocity around -1 V with regard to the negative differential mobility at increased electric fields. Therefore, considering non-equilibrium transport simulations as provided by the EB-model prove to be an important tool for designing THz-PD structures. Future fabrications will utilize such transient dynamics to further enhance the speed and stability for high-power operation.

An important feature of the PDs presented in this work is the excellent saturation characteristic, which is shown in Fig. 12 for several PD lengths. Due to the particular design of the electric field distribution, saturation only takes place for very high photocurrents contributed by the charge compensated layers. This behavior was illustrated in Fig. 1 in Section 2, where the electrical field approaches a rather homogeneous distribution allowing an optimized carrier transport. Another important factor is the higher responsivity together with more advantageous optical properties in the longer PDs as shown in Fig. 8. Due to the evanescent coupling behavior the PD lengths of $12 \mu\text{m}$ and $17 \mu\text{m}$ offer a more evenly distributed optical intensity within the active absorber region.

Such waveguide integrated PDs approach the ideal case of uniform illumination usually achieved in vertical PDs featuring optimal working conditions for a larger volume ratio. Thanks to the E-field management, fast carrier transport is still enabled at high optical input power. Thus, one of the advantages presented in this work is to employ waveguide type PDs for uniform carrier generation over a large absorption region, which facilitates extremely high saturation currents

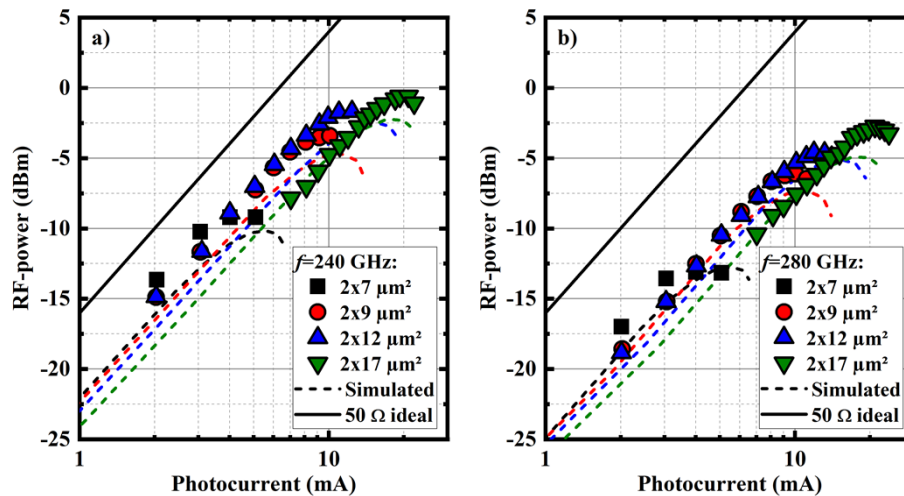


Fig. 12. Measured saturation characteristics for several photodiode geometries at 240 GHz and 280 GHz. The corresponding simulations (dashed lines) are in good agreement with the saturation currents and saturated output powers. Highest output powers are provided by the PD with a geometry of $2 \times 17 \mu\text{m}^2$ while achieving high photocurrents around 20 mA.

and therefore maximized RF-power. As a result, the obtainable power for long WGPDs remains higher even far beyond their RC-cutoff frequency than compared to smaller WGPDs despite their reduced RC-limitation. Consequently, saturation for the $17 \mu\text{m}$ long PD does not take place for photocurrents below 20 mA at 240 GHz and 280 GHz. Such behavior indicates a successful design of the electric field distribution for high optical input powers maintaining sufficiently fast carrier transport.

Together with the high stability of the electric field and the good responsivity of about 0.25 A/W, the saturation characteristic in Fig. 12 reveals very high output powers of -0.6 dBm at 240 GHz and -2.7 dBm at 280 GHz. In comparison, the shorter PDs offer a slightly higher output power due to their increased RC-cutoff frequency before saturation takes place. However, saturation occurs already for much smaller photocurrents resulting in an overall lower output power for the PD with a length of $7 \mu\text{m}$. This is related to the inhomogeneous distribution of optical intensity at the end of the PD resulting in a local power saturation while the remaining sections receive almost no optical power. The described behavior is in good agreement with the simulated PD geometries including electrical and optical simulations shown as dashed lines.

4.5. Ultra-broadband characteristics

To characterize the broadband capabilities and transit time limitation of the layer system, WG-PDs were integrated with 90° bow-tie (BT) antennas. This allows to reach higher frequencies, without the restriction of the CPW and the related RF-probes. The photonic chip was mounted on a highly resistive hyper-hemispherical silicon lens. On receiver side, a commercial broadband SBD (ACST 3DL 12CLS2500 A1), also with a silicon lens port, was used for THz-detection. In Fig. 13(a) and (b), an optical microscope picture of a BT-PD and the corresponding frequency response are shown. The measured device features a geometry of about $6 \times 6 \mu\text{m}^2$ and was characterized at a photocurrent of 3 mA obviating saturation effects for the given size.

For frequencies above 200 GHz, a decreasing of power with a slope of $1/f^{-4}$ is observed indicating an additional frequency limitation related to the transit time. This reveals a cutoff frequency, which is in the range of the transit time limitation predicted by our EB-model TCAD simulation being about 250 GHz. A frequency limited contribution due to substrate modes

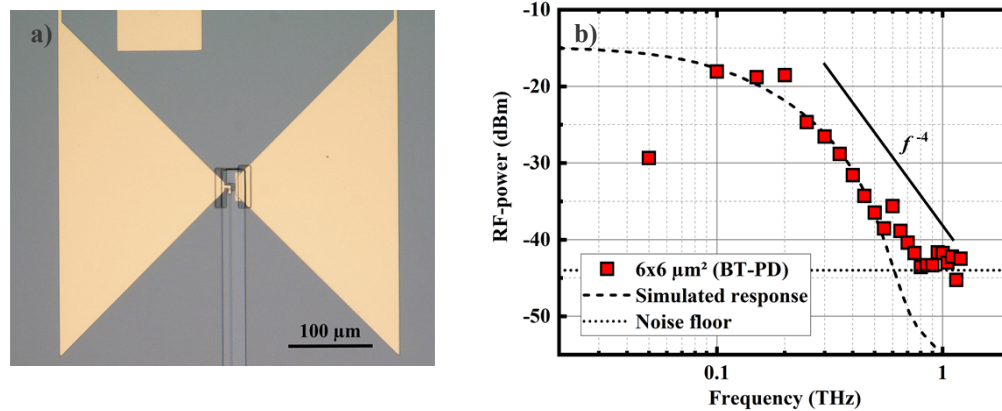


Fig. 13. Optical microscope picture of a bowtie-antenna integrated photodiode (BT-PD) for THz-power measurements in a), using a UWB SBD detector. At a reverse bias of 1.2 V the photocurrent was set to 3 mA. The measured frequency response in b) (red squares) indicates an additional transit time limitation around 250 GHz. The simulated frequency response (dashed line) matches the experimental data below 0.7 THz. At higher frequencies the measured output power approaches the noise floor of the detector.

can be neglected in this case since reflection at the interface between InP-substrate and silicon are insignificant. The simulated response, visible as a dashed line in Fig. 13(b), matches the measured trajectory until a frequency of 0.7 THz before the obtainable RF-power falls below the noise level of around -44 dBm for the given detector.

Finally, the ultra-broadband capability of the layer structure itself can be revealed in Fig. 13 by combining two separate measurements into a single frequency response. Here the measured relative response from CPW-integrated and bowtie integrated PDs are compared with the simulated transit time limited response from TCAD simulations. This has been achieved by

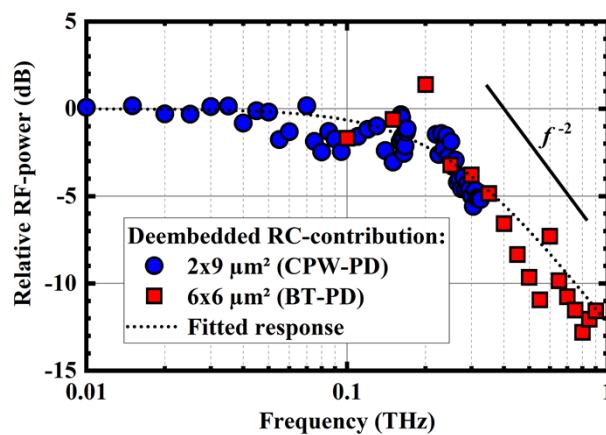


Fig. 14. Relative RF-power for the whole frequency region (DC-THz) from both the bow-tie antenna integrated photodiode (red squares) and a CPW-integrated photodiode (blue circles) after their RC-characteristics have been deembedded. The fitted frequency response (dotted line) indicates a cutoff at 249 GHz, which confirms the simulated response with a transit time limited cutoff frequency of 254 GHz.

deembedding the RC-characteristic of each design, which allows to illustrate the complete frequency response until 1.2 THz.

While the frequency response obtained from the deembedded CPW-integrated PD exhibits a power variation of a couple dB, it reveals a continuous trend with the deembedded broadband antenna measurement. Similar to the $1/f^{-4}$ slope in Fig. 13(b), indicating both RC-time and transit time limitation, the trend in Fig. 14 reveals a $1/f^{-2}$ slope, which relates to the carrier delay time only. Fitting the overall response with the delay time related equivalent circuit in Fig. 6(a) results in a cutoff frequency of 249 GHz, which is in the range of the transit time limited frequency of 254 GHz in Section 2 obtained by simulations.

5. Conclusion

Optimizing the electric field distribution in the junction region of a waveguide-type MUTC-PD for high optical intensities has allowed pushing the saturation photocurrent up to over 20 mA at 280 GHz. To our knowledge, the attained RF-output power close to 0 dBm represents the highest output power ever achieved in the WR3.4 band for non-resonant MUTC-PDs with CPW output. Furthermore, fabricated waveguide-type MUTC-PDs with on-chip integrated bow-tie antennas reveal ultra-wideband capabilities up to 0.7 THz. With the aid of energy-balance (EB) simulations, the layer structure and doping profile of the waveguide type MUTC-PDs were optimized for achieving both, high frequencies and high output power levels. It is shown theoretically that the consideration of the transient carrier dynamics in the EB model is crucial as it enables the accurate analysis of the MUTC-PD performances, which cannot be achieved using the drift-diffusion model. Consequently, the measured THz output power versus DC bias agrees well with the simulations, which proves the accuracy of the developed EB model. Another key improvement for reaching a high THz output power is the improved evanescent optical coupling efficiency between the passive optical waveguide and the absorbing region. This allows a high absorption efficiency even for comparably short waveguides. Quantitatively, a sensitivity of 0.25 A/W was achieved for a 16 μm long waveguide.

The reported work is an important step towards versatile photonic THz components because the developed waveguide-type THz photodiodes enable a straightforward implementation in photonic integrated circuits (PICs). In future works, a fabrication process utilizing reactive ion etching (RIE) will be developed to yield a more precise definition of the PD's lateral geometries and increase reproducibility. This allows for example the integration of multiple waveguide-type MUTC-PDs with THz antenna arrays and optical beam forming networks for photonic assisted beam-steering in future mobile THz communications and sensing applications.

Funding. Deutsche Forschungsgemeinschaft (Project-ID 287022738– CRC/TRR 196); Bundesministerium für Bildung und Forschung (6GEM, grant No.16KISK039, NRW/EFRE THzIZ, grant No. EFRE-0400215, Open6GHub, grant No.16KISK017).

Acknowledgements. The authors would like to thank the researchers at the Necmettin Erbakan University, Science and Technology Research and Application Center (BiTAM), Konya, Turkey for performing measurements with their scanning electron microscope. This work was supported by the Deutsche Forschungsgemeinschaft (DFG, German Research Foundation) – TRR 196 MARIE under Grant 287022738 (projects C02, C06 and C07).

Disclosures. The authors declare no conflicts of interest.

Data availability. Data underlying the results presented in this paper are not publicly available at this time but may be obtained from the authors upon reasonable request.

References

1. T. Ishibashi, S. Kodama, N. Shimizu, and T. Furuta, "High-speed response of uni-traveling-carrier photodiodes," *Jpn. J. Appl. Phys.* **36**(10R), 6263 (1997).
2. T. Nagatsuma, H. Ito, and T. Ishibashi, "High-power RF-photodiodes and their applications," *Laser Photonics Rev.* **3**(1-2), 123–137 (2009).
3. T. Kurokawa, T. Ishibashi, M. Shimizu, K. Kato, and T. Nagatsuma, "Over 300 GHz bandwidth UTC-PD module with 600 GHz band rectangular-waveguide output," *Electron. Lett.* **54**(11), 705–706 (2018).

4. M. Ali, J. M. Pérez-Escudero, R. C. Guzmán-Martínez, M. C. Lo, I. Ederra, R. Gonzalo, L. E. García-Muñoz, G. Santamaría, D. Segovia-Vargas, F. van Dijk, and G. Carpintero, "300 GHz optoelectronic transmitter combining integrated photonics and electronic multipliers for wireless communication," *Photonics* **6**(2), 35 (2019).
5. S. Dülme, M. Steeg, I. Mohammad, N. Schirnski, J. Tebart, and A. Stöhr, "Ultra-low phase-noise photonic terahertz imaging system based on two-tone square-law detection," *Opt. Express* **28**(20), 29631–29643 (2020).
6. H. Ito and T. Ishibashi, "Photonic terahertz-wave generation using slotantenna-integrated uni-traveling-carrier photodiodes," *IEEE J. Sel. Top. Quantum Electron.* **23**(4), 1–7 (2017).
7. P. Lu, T. Haddad, J. Tebart, M. Steeg, B. Sievert, J. Lackmann, A. Rennings, and A. Stöhr, "Mobile THz communications using photonic assisted beam steering leaky-wave antennas," *Opt. Express* **29**(14), 21629–21638 (2021).
8. T. Haddad, C. Biurrun-Quel, P. Lu, J. Tebart, B. Sievert, S. Makhlof, M. Grzeslo, J. Teniente, C. Del-Rio, and A. Stöhr, "Photonic-assisted 2-D terahertz beam steering enabled by monolithically integrated LWAs array and BFN," *Opt. Express* **30**(21), 38596–38612 (2022).
9. I. D. Henning, M. J. Adams, Y. Sun, D. G. Moodie, D. C. Rogers, P. J. Skuse, and R. J. Firth, "Broadband antenna-integrated, edge-coupled photomixers for tuneable terahertz sources," *IEEE J. Quantum Electron.* **46**(10), 1498–1505 (2010).
10. M. Che, Y. Matsuo, H. Kanaya, H. Ito, T. Ishibashi, and K. Kato, "Optoelectronic THz-wave beam steering by arrayed photomixers with integrated antennas," *IEEE Photonics Technol. Lett.* **32**(16), 979–982 (2020).
11. E. Rouvalis, M. Chtioui, M. Tran, F. Lelarge, F. van Dijk, M. J. Fice, C. C. Renaud, G. Carpintero, and A. J. Seeds, "High-speed photodiodes for InP-based photonic integrated circuits," *Opt. Express* **20**(8), 9172–9177 (2012).
12. S. M. M. Rahman, H. Hjelmgren, J. Vukusic, J. Stake, P. A. Andrekson, and H. Zirath, "Hydrodynamic simulations of untraveling-carrier photodiodes," *IEEE J. Quantum Electron.* **43**(11), 1088–1094 (2007).
13. C. Gardes, J. Justice, F. Gity, H. Yang, and B. Corbett, "Numerical simulations with energy balance model for untraveling-carrier photodiode," *2015 IEEE 15th International Conference on Nanotechnology (IEEE-NANO)*, IEEE, pp. 350–353, 2015.
14. L. Guoyu, Z. Yejin, L. Xiaojian, and T. Lilin, "Structure optimization of a uni-traveling-carrier photodiode with introduction of a hydro-dynamic model," *J. Semicond.* **31**(10), 104005 (2010).
15. V. Rymanov, A. Stöhr, S. Dülme, and T. Tekin, "Triple transit region photodiodes (trr-pds) providing high millimeter wave output power," *Opt. Express* **22**(7), 7550–7558 (2014).
16. J. Li, B. Xiong, C. Sun, and Y. Luo, "Dual-drifting-layer uni-traveling carrier photodiode for wide bandwidth and high power performance," *CLEO: Sci. Innov., J. Opt. Soc. Am.*, 2015.
17. L. Zheng, X. Zhang, Y. Zeng, S. R. Tatavarti, S. P. Watkins, C. R. Bolognesi, S. Demiguel, and J. C. Campbell, "Demonstration of high-speed staggered lineup GaAsSb-InP untraveling carrier photodiodes," *IEEE Photonics Technol. Lett.* **17**(3), 651–653 (2005).
18. E. Rouvalis, F. Pozzi, R. Steed, C. C. Renaud, and A. J. Seeds, "A travelling-wave uni-travelling photodiode for continuous wave terahertz generation," *London Communications Symposium*, 2009.
19. J. W. Shi, F. M. Kuo, and J. E. Bowers, "Design and analysis of ultra-high-speed near-ballistic uni-traveling-carrier photodiodes under a 50-ohm load for high-power performance," *IEEE Photonics Technol. Lett.* **24**(7), 533–535 (2012).
20. H. Pan, A. Beling, H. Chen, J. C. Campbell, and P. D. Yoder, "The influence of nonlinear capacitance and responsivity on the linearity of a modified uni-traveling carrier photodiode," *International Topical Meeting on Microwave Photonics jointly held with the 2008 APMP Conference*, IEEE, 2008.
21. B. Vidal, T. Nagatsuma, N. J. Gomes, and T. E. Darcie, "Photonic technologies for millimeter-and submillimeter-wave signals," *Adv. Opt. Technol.* **2012**, 1 (2012).
22. E. Rouvalis, C. C. Renaud, D. G. Moodie, M. J. Robertson, and A. J. Seeds, "Traveling-wave uni-traveling carrier photodiodes for continuous wave THz generation," *Opt. Express* **18**(11), 11105–11110 (2010).
23. P. Latzel, F. Pavanello, M. Billet, S. Bretin, A. Beck, M. Vanwollegem, C. Coinon, X. Wallart, E. Peytavit, G. Ducournau, and M. Zaknoune, "Generation of mW level in the 300-GHz band using resonant-cavity-enhanced untraveling carrier photodiodes," *IEEE Trans. Terahertz Sci. Technol.* **7**(6), 800–807 (2017).
24. C. Barrientos, V. Calle, F. P. Mena, J. Vukusic, J. Stake, and E. A. Michael, "Vertically illuminated TW-UTC photodiodes for terahertz generation," *Proc. SPIE* **8452**, 84522I (2012).
25. Q. Li, K. Sun, K. Li, Q. Yu, P. Runge, W. Ebert, A. Beling, and J. C. Campbell, "High-power evanescently coupled waveguide MUTC photodiode with >105-GHz bandwidth," *J. Lightwave Technol.* **35**(21), 4752–4757 (2017).
26. E. Rouvalis, C. C. Renaud, D. G. Moodie, M. J. Robertson, and A. J. Seeds, "Continuous wave terahertz generation from ultra-fast inp-based photodiodes," *IEEE Trans. Microw. Theory Tech.* **60**(3), 509–517 (2012).
27. T. G. Sanchez, J. V. Perez, P. G. Conde, and D. P. Collantes, "Electron transport in InP under high electric field conditions," *Semicond. Sci. Technol.* **7**(1), 31–36 (1992).
28. M. Natrella, C. P. Liu, C. Graham, F. van Dijk, H. Liu, C. C. Renaud, and A. J. Seeds, "Modelling and measurement of the absolute level of power radiated by antenna integrated THz UTC photodiodes," *Opt. Express* **24**(11), 11793–11807 (2016).
29. J. Li, B. Xiong, C. Sun, D. Miao, and Y. Luo, "Analysis of frequency response of high power MUTC photodiodes based on photocurrent-dependent equivalent circuit model," *Opt. Express* **23**(17), 21615–21623 (2015).
30. G. Wang, T. Tokumitsu, I. Hanawa, Y. Yoneda, K. Sato, and M. Kobayashi, "A time-delay equivalent-circuit model of ultrafast pin photodiodes," *IEEE Trans. Microw. Theory Tech.* **51**(4), 1227–1233 (2003).